

Mechanical and thermodynamical properties of $\beta - Cu - Al - Mn$ alloys along the $Cu_3Al \rightarrow Cu_2AlMn$ compositional line

Alejandro Alés^{1,2} and Fernando Lanzini^{1,2}

¹*Instituto de Física de Materiales Tandil (IFIMAT), Universidad Nacional del Centro de la Provincia de Buenos Aires (UNCPBA), Pinto 399, 7000 Tandil, Argentina*

²*Consejo Nacional de Investigaciones Científicas y Técnicas (CONICET), Argentina*

Abstract

The elastic properties of $Cu - Al - Mn$ alloys with compositions along the $Cu_3Al \rightarrow Cu_2AlMn$ line and *bcc*-based structures, are studied by means of first-principles calculations. From the calculated elastic constants, the Zener's anisotropy, sound velocities and Debye temperature are determined. The theoretical results compare well with the available experimental data. The influence of vibrations is introduced through the quasi-harmonic Debye model, and different properties are studied as functions of temperature and composition.

Keywords— Cu-Al-Mn, First-Principles Calculations, Elastic Constants, Debye Temperature, Quasi-Harmonic Approximation

1 Introduction

Shape memory alloys (SMAs) have attracted attention in the last decades due to their interesting mechanical properties (pseudoelasticity, shape memory effect, double shape memory effect) (1). These mechanical properties are associated with a diffusionless martensitic transformation (2). *Cu*-based alloys are particularly interesting due to their lower cost and comparatively good shape memory properties (3). In these systems, the martensitic transformation takes place from a metastably retained β phase, with *bcc* structure, to a martensitic phase with close-packed structure. One of such *Cu*-based SMAs is the $Cu - Al - Mn$ system: the use of this family of alloys in seismic applications (4–7) as well as in medicine, aeronautics and robotics (8–12) has been subject of extensive research in the last years.

The $Cu - Al - Mn$ system presents some advantageous properties as compared to other *Cu*-based shape memory alloys. The addition of *Mn* increases the range of stability of the β phase. Besides, the presence of *Mn* confers magnetic properties, as a result of the coupling between the magnetic moments located at the *Mn* sites. For instance, the Heusler alloy with stoichiometric composition Cu_2AlMn has a ferromagnetic to paramagnetic transition with a high Curie temperature $T_C \approx 630K$ (13). Other interesting feature is the formation of a miscibility gap at temperatures around $600K$ and below, for compositions along the pseudobinary line $Cu_3Al \rightarrow Cu_2AlMn$ (14–18). This two-phases gap is formed by a spinodal decomposition mechanism, giving place to regions with composition close to Cu_3Al and DO_3 structure, and others with composition near Cu_2AlMn and $L2_1$ order (18–23). The Cu_3Al regions are paramagnetic, whereas the $L2_1$ ones are ferromagnetic. Although the nature of the gap is still a matter of discussion, it is known that the difference in lattice parameters between the phases leads to internal tensions that could partly explain the decomposition (14, 18, 20). In a previous work (24) it has been shown that there is also magnetic reasons behind this decomposition.

The aim of this work is to characterize, using first-principles methods and the quasiharmonic approximation (QHA),

the elastic, vibrational and thermodynamic properties of alloys along the $Cu_3Al \rightarrow Cu_2AlMn$ line of compositions. This will allow to gain insight about the reasons leading to the formation of the miscibility gap.

The rest of this work is organized as follows: in section 2 the computational details of the first principles calculations are explained, and the main equations of the QHA are introduced. In section 3 the results are presented and discussed, and the main conclusions are outlined in section 4.

2 Methodology

2.1 First-principles calculations

First-principles calculations were performed by means of the Quantum Espresso implementation (25, 26). This is an integrated suite of computational codes based on the density functional theory (DFT) (27, 28), and employs an expansion of plane waves and pseudopotentials. In the present work, the ionic cores for Cu , Al and Mn were described by Vanderbilt ultrasoft pseudopotentials (29). The exchange-correlation term of the spin-polarized calculations was represented by the Perdew-Burke-Ernzerhof implementation of the generalized gradient approximation (GGA) (30). A careful examination of the energy convergence respect to different control parameters was performed prior to the self-consistent calculations. The energy cut-off for the plane wave expansion was established in 40 Ry, and for the charge density in 480 Ry; a uniform mesh of $10 \times 10 \times 10$ k points, automatically generated according to a Monkhorst-Pack scheme was employed (31). The convergence criteria in the total energy for the self-consistent cycle was set to 1×10^{-8} Ry.

As postulated by other authors (32, 33) and verified in a previous work (24), the magnetic contributions from Cu and Al atoms are negligible; then, the spin-polarized calculations were performed assuming that the magnetic moments are due solely to Mn atoms.

Five alloys along the line of compositions $Cu_3Al \rightarrow Cu_2AlMn$ were studied. Description of these structures can be made with the help of Figure 1. In the limiting Cu_3Al alloy with DO_3 order, sublattices I , II and III are occupied by Cu atoms and sublattice IV by Al . In the Heusler Cu_2AlMn alloy with $L2_1$ order, sublattices I and II are occupied by Cu , sublattice III by Mn , and sublattice IV by Al . Besides these limiting cases, three ordered compounds with compositions $Cu_{11}Al_4Mn_1$, $Cu_{10}Al_4Mn_2$ and $Cu_9Al_4Mn_3$ were also studied (note that all the considered alloys possess a fixed aluminum content of 25 at. %). The three intermediate systems, with 16 atoms per unit cell, were constructed starting from Cu_3Al and replacing, respectively, 1, 2 or 3 Cu atoms in the sublattice III (Fig. 1) by Mn atoms. The corresponding compositions lie equidistantly between Cu_3Al and Cu_2AlMn . The resulting structures can be regarded as partially ordered $L2_1$ structures.

For each of the studied alloys, a structural optimization varying the cubic lattice parameter was done. The equilibrium state was determined by locating the minimum of the energy as a function of the lattice parameter, fitting the calculated data with a Murnaghan equation of state (EOS) (34). From these fittings, the energy per formula unit E_0 , the equilibrium volume V_0 , the equilibrium bulk modulus B_0 and its pressure derivative B'_0 , were obtained.

2.2 Determination of the elastic constants

In a cubic system there are only three independent elastic constants, namely C_{11} , C_{12} and C_{44} . Determination of the elastic constants is performed by applying different distortions to the cubic cell. The bulk modulus B_0 and the equilibrium volume V_0 are obtained by fitting the Murnaghan EOS (34), and correspond to an hydrostatic variation of volume by means the following perturbation of the basis vectors of the lattice

$$D(\delta) = \begin{pmatrix} 1 + \delta & 0 & 0 \\ 0 & 1 + \delta & 0 \\ 0 & 0 & 1 + \delta \end{pmatrix}$$

where δ is the magnitude of the strain. B_0 is related with the elastic constants by the expression

$$B_0 = \frac{C_{11} + 2C_{12}}{3} \quad (1)$$

The combination $C_{11} - C_{12}$ is obtained by performing a volume-conserving orthorhombic strain (35, 36)

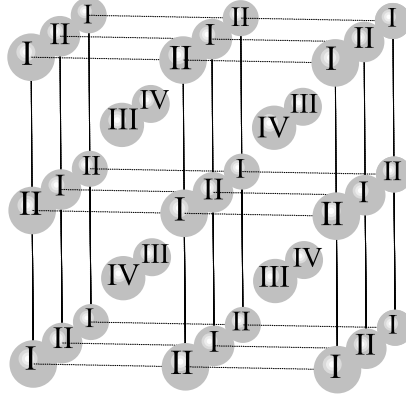


Figure 1: Body centered cubic supercell subdivided in four interpenetrating fcc sublattices

$$D(\delta) = \begin{pmatrix} 1 + \delta & 0 & 0 \\ 0 & 1 - \delta & 0 \\ 0 & 0 & \frac{1}{1 - \delta^2} \end{pmatrix}$$

and fitting to the change in energy with respect to the unstrained crystal

$$\Delta E(\delta) = \Delta E(-\delta) = V_0(C_{11} - C_{12})\delta^2 + O(\delta^4) \quad (2)$$

The combination of Eqs. (1) and (2) allows calculating C_{11} and C_{12} . The remaining elastic constant, C_{44} , is obtained by applying a volume-conserving monoclinic distortion

$$D(\delta) = \begin{pmatrix} 1 & \frac{\delta}{2} & 0 \\ \frac{\delta}{2} & 1 & 0 \\ 0 & 0 & \frac{4}{4 - \delta^2} \end{pmatrix}$$

In this case, the difference in energy respect to the relaxed lattice is expressed as

$$\Delta E(\delta) = \Delta E(-\delta) = \frac{1}{2}V_0C_{44}\delta^2 + O(\delta^4) \quad (3)$$

In the present work, ten distortions of each type (orthorhombic or monoclinic), with values $\pm 1\%$, $\pm 2\%$, $\pm 3\%$, $\pm 4\%$ and $\pm 5\%$, were applied to the relaxed cubic structure with volume V_0 .

From the values of the elastic constants the shear modulus is obtained. We will use the Hill method (37), according to which the shear modulus G_H is given by the average

$$G_H = \frac{G_v + G_r}{2}, \quad (4)$$

where G_v is the Voigt's estimate (38):

$$G_v = \frac{C_{11} - C_{12} + 3C_{44}}{5} \quad (5)$$

and G_r is the Reuss value (39)

$$G_r = \frac{5(C_{11} - C_{12})C_{44}}{3(C_{11} - C_{12}) + 4C_{44}} \quad (6)$$

The isotropic Young modulus, E , and Poisson ratio, ν , are given by

$$E = \frac{9B_0G_H}{3B_0 + G_H} \quad (7)$$

$$\nu = \frac{3B_0 - 2G_H}{2(3B_0 + G_H)} \quad (8)$$

2.3 Thermal properties

The vibrational motion of the lattice was incorporated through the quasi-harmonic Debye model, as implemented in the software GIBBS (40). Taking as input the ab-initio values of $E(V)$ for the hydrostatic variation of volume and the Poisson ratio ν , Eq. (8), the adiabatic bulk modulus is computed by means of the derivative

$$B_S \approx V \frac{d^2 E(V)}{dV^2} \quad (9)$$

and then the volume-dependent Debye temperature is obtained

$$\Theta_D = \frac{\hbar}{k} [6\pi^2 V^{1/2} n]^{1/3} \left(\frac{B_S}{M} \right)^{1/2} f(\nu) \quad (10)$$

where

$$f(\nu) = \left\{ 3 \left[2 \left(\left(\frac{2}{3} \right) \frac{1+\nu}{1-2\nu} \right)^{3/2} + \left(\left(\frac{1}{3} \right) \frac{1+\nu}{1-\nu} \right)^{3/2} \right]^{-1} \right\}^{1/3}$$

The thermal evolution of different properties can be evaluated by constructing the Gibbs free energy as

$$G(V, P, T) = E(V) + PV + A_{vib}(\theta_D(V); T) \quad (11)$$

being A_{vib} the vibrational contribution

$$A_{vib} = nk_B T \left[\frac{9}{8} \frac{\Theta_D}{T} - 3 \log \left(1 - e^{-\frac{\Theta_D}{T}} \right) - D \left(\frac{\Theta_D}{T} \right) \right] \quad (12)$$

with $D \left(\frac{\Theta_D}{T} \right)$ being the third-order Debye integral, n the number of atoms in the unitary cell and k_B the Boltzmann's constant. At given (p, T) the equilibrium volume is found from the condition

$$\left(\frac{\partial G(V, P, T)}{\partial V} \right)_{p, T} = 0 \quad (13)$$

After that, it is possible to calculate other properties such as the isothermal bulk modulus

$$B_T(p, T) = -V \left(\frac{\partial^2 G(V, P, T)}{\partial V^2} \right)_{p, T} \quad (14)$$

the vibrational heat capacity

$$C_v = 3nk_B \left[4D \left(\frac{\Theta_D}{T} \right) - \frac{3 \frac{\Theta_D}{T}}{e^{\frac{\Theta_D}{T}} - 1} \right] \quad (15)$$

and the volumetric thermal expansion coefficient

$$\alpha = \frac{\gamma C_v}{B_T V} \quad (16)$$

where γ is the Grüneisen parameter, obtained through the Mie-Grüneisen equation (40, 41).

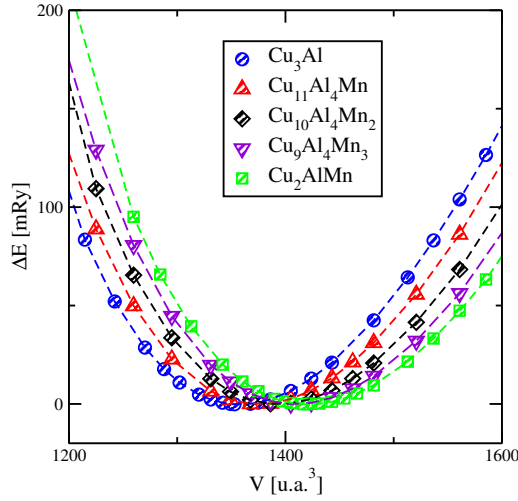


Figure 2: Energy difference from the equilibrium volume as function of the volume for different compositions. The dashed line corresponds to the Murnaghan fit.

3 Results and discussion

3.1 Elastic and acoustic properties

In Figures 2 - 4, the changes in energy in reference to the equilibrium volume for different strains and alloy compositions are shown. The hydrostatic changes of volume shown in Fig. 2 were fitted by the Murnaghan EOS for each alloy, determining the corresponding values of V_0 and B_0 . These values are listed in Table 1. When orthorhombic strains are applied (Fig. 3), the variation of energy with δ is more markedly composition dependent than for the monoclinic strains (Fig. 4), where the curves for different compositions almost overlap. This implies that the $C_{11} - C_{12}$ difference varies more with composition than the C_{44} value. Furthermore, the difference $C_{11} - C_{12}$ has a monotonous behavior respect the copper contents.

The values of the elastic constants obtained through Eqs. 1 - 3 are listed in Table 1. Experimental values and theoretical calculations taken from the literature are included for comparison. For the Heusler alloy Cu_2AlMn , our results agree well with the experimental determinations by Michelutti et al (42) (values extrapolated to $0K$), as well as with recent theoretical calculations using full-potential linearized augmented plane waves (FPLAPW) (43, 44) and the projector augmented wave method (PAW) (45). For the intermediate compositions, the elastic constants have been experimentally determined for alloys $Cu - 25\%Al - 5at.\%Mn$ (at temperatures above the martensitic transformation) and for $Cu - 25at.\%Al - 7.5at.\%Mn$ and $Cu - 25at.\%Al - 10at.\%Mn$ (above liquid nitrogen) (46). Extrapolation of these experimental results to $0K$ are also listed in Table 1.

In Fig 5, the values of B_0 , C_{44} and C' are shown as a function of the Mn content, where

$$C' = \frac{C_{11} - C_{12}}{2}$$

is the elastic modulus related to $\langle 110 \rangle \langle 1\bar{1}0 \rangle$ shear. All the alloys satisfy the Born stability criteria, $B_0 > 0$, $C_{44} > 0$, and $C' > 0$. Experimental values in other $Cu - Al$ based systems possess values in the same range than the ones calculated here. For instance, for $Cu - Al - Be$ with Be contents between $2.5 - 5at.\%$, the room temperature values are in the ranges $B_0 \approx 125 - 130 GPa$, $C_{44} \approx 90 - 95 GPa$, and $C' \approx 7 - 9 GPa$ (47). For $Cu - Al - Ni$, $B_0 \approx 127 - 133 GPa$, $C_{44} \approx 95 GPa$ and $C' \approx 7.34 - 7.48 GPa$ (48). In the compilation by Romero and Pelegrina (49) for $Cu - Zn$, $Cu - Al - Zn$, $Cu - Al - Be$ and $Cu - Al - Ni$ alloys, C_{44} ranges between around 95 and 105 GPa at different temperatures.

As shown in Fig. 5, C' has a low value as compared to the other two moduli in all the range of compositions and

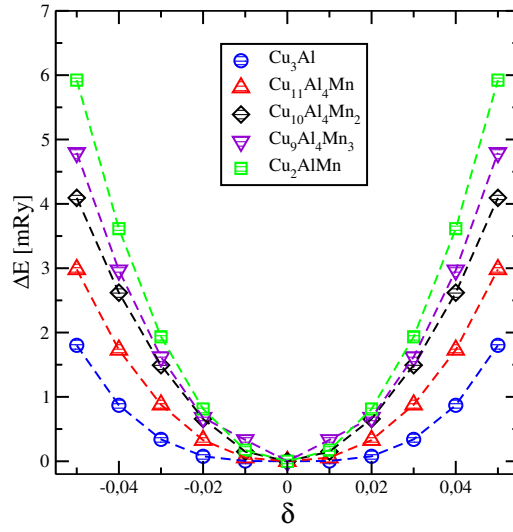


Figure 3: Energy differences for orthorhombic deformations δ and the different compositions. The dashed lines are just guides for eyes.

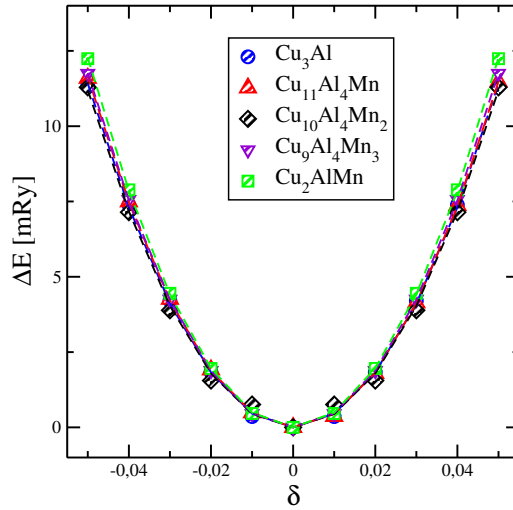


Figure 4: Energy difference for monoclinic deformations δ and for the different compositions. The dashed lines are just guides for eyes.

decreases with the amount of copper in the alloy. The comparatively low values of C' indicate that the bcc structure has weak restoring forces for shears in the $\{110\}$ planes along the directions $\langle 1\bar{1}0 \rangle$ (50) and play an important role in the occurrence of the martensitic transformation (51).

The Young and shear moduli, and the Poisson ratio, obtained by Eqs. 4 - 8 are listed in Table 2. For Cu_2AlMn our results closely compares with those of Ref. (45). It should be noted that both the Young and shear moduli increases and the value of Poisson ratio decreases when the manganese content grows.

Alloy	Ref.	$V_0[ua^3]$	$B_0[GPa]$	$C_{11}[GPa]$	$C_{12}[GPa]$	$C_{44}[GPa]$
Cu_3Al	This work	84.84348	131.23	137.23	128.03	99.08
$Cu_{70}Al_{25}Mn_5$	(46), experimental	---	129.33	140.0	124.0	98
$Cu_{11}Al_4Mn$	This work	85.9660	128.11	135.97	124.35	99.03
$Cu_{67.5}Al_{25}Mn_{7.5}$	(46), experimental	---	128.0	138.0	123.0	104
$Cu_{10}Al_4Mn_2$	This work	87.1304	123.54	134.73	117.94	94.59
$Cu_{65}Al_{25}Mn_{10}$	(46), experimental	---	128.0	138.0	123.0	104
$Cu_9Al_4Mn_3$	This work	88.0784	121.67	134.12	115.44	98.34
Cu_2AlMn	This work	88.8360	120.51	138.8	111.3	102.0
	(42), experimental ¹	89.4498	110.4	128.1	101.5	104.4
	(43), FPLAPW	88.1167	125.3	143.7	116.1	117.6
	(44), FPLAPW	---	122.3	137.0	115.0	112
	(45), PAW	88.44086	122.2	138.8	113.9	103.0

Table 1: Equilibrium volume per atom, bulk modulus, and elastic constants for the different alloys.

Alloy	$E[GPa]$	$G_H[GPa]$	ν	A^C	B_0/G	C_{12}/C_{44}	$\Theta_{D,0}[K]$
Cu_3Al	99.00	36.02	0.374	24.17	3.64	1.29	322.14
$Cu_{11}Al_4Mn$	102.61	37.54	0.367	17.04	3.41	1.26	330.57
$Cu_{10}Al_4Mn_2$	106.63	39.31	0.356	11.27	3.14	1.25	340.56
$Cu_9Al_4Mn_3$	112.00	41.59	0.346	10.53	2.93	1.17	351.97
Cu_2AlMn	126.12	47.57	0.325	7.44	2.53	1.09	378.18
$Cu_2AlMn(45)$	123.9	46.6	0.331	7.68	2.63	1.11	375.40

Table 2: Calculated Young and shear moduli, Poisson ratio, anisotropy, ductility, Cauchy relations and Debye temperature at the equilibrium volume at $T = 0K$

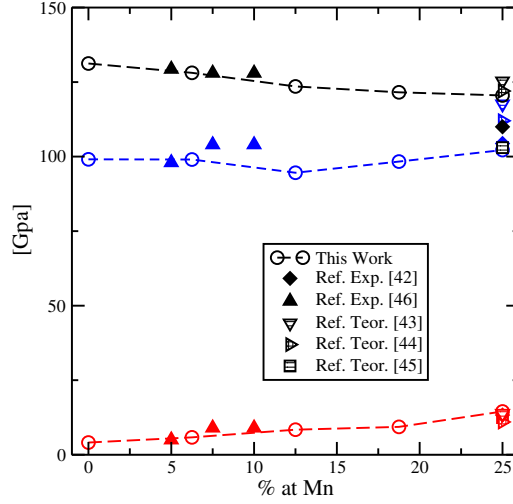


Figure 5: Elastic moduli as a function of Mn content. Code color: Black for Bulk modulus, Blue for C_{44} and red for C' . In empty circles, the present work results.

The anisotropies of alloys crystals, A^C , calculated as the Zener ratio (52):

$$A^C = \frac{C_{44}}{C'}$$

are also listed in Table 2. The low values of C' lead to high values of the anisotropy. According to the compilation of experimental data by Z. Lethbridge et al. (53), all cubic materials with $A^C > 4$ show a negative Poisson's ratio in some combination of load direction / transversal plane. Materials with negative Poisson's ratio are called auxetics (54), and have the property of displaying a widening upon application of a longitudinal tensile strain. Around 69 % of the elemental cubic metals possess negative Poisson's ratio when stretched along the $[110]$ direction (55). In a recent work (56) it has been shown that an alloy of composition $Cu - 16.9Al - 11.6Mn$ (at. %) possesses a negative Poisson's ratio along the $[110]$ direction when the strain is measured along the transverse $[1\bar{1}0]$ direction: $\nu_{\langle[110],[1\bar{1}0]\rangle} = -0.51$, and a large and positive Poisson's ratio when the strain is measured along the $[001]$ transverse direction: $\nu_{\langle[110],[001]\rangle} = 1.34$. Using the elastic constants obtained in the present calculations these Poisson's ratios can be calculated through the relations (55):

$$\nu_{\langle[110],[1\bar{1}0]\rangle} = \frac{-2C_{11}C_{44} + (C_{11} - C_{12})(C_{11} + 2C_{12})}{2C_{11}C_{44} + (C_{11} - C_{12})(C_{11} + 2C_{12})}$$

$$\nu_{\langle[110],[001]\rangle} = \frac{4C_{12}C_{44}}{2C_{11}C_{44} + (C_{11} - C_{12})(C_{11} + 2C_{12})}$$

The obtained values are detailed in Table 3. The present values are in the range of the experimental data.

The anisotropy is also related to the spinodal decomposition process. For $A^C > 1$, spinodal decomposition gives rise to compositional plane waves on $\{100\}$ planes, whereas for $A^C < 1$ this occurs on $\{111\}$ planes (57, 58). For the alloys studied in this work, the prediction of $A^C > 1$ agrees with the experimental observation of composition modulations along the $\langle 100 \rangle$ direction (59).

Comp.	$\nu_{\langle[110],[\bar{1}\bar{1}0]\rangle}$	$\nu_{\langle[110],[001]\rangle}$
Cu_3Al	-0.79	1.67
$Cu_{11}Al_4Mn$	-0.72	1.57
$Cu_{10}Al_4Mn_2$	-0.61	1.41
$Cu_9Al_4Mn_3$	-0.59	1.37
Cu_2AlMn	-0.48	1.19

Table 3: Poisson's ratio for loads applied in the $[110]$ direction and strains along the transverse directions $[\bar{1}\bar{1}0]$ and $[001]$.

Alloy	Ref.	$v_l[m/s]$	$v_t[m/s]$	$v_{eff}[m/s]$
Cu_3Al	This work	5002.1	2242.2	2529.3
$Cu_{11}Al_4Mn$	This work	5029.2	2308.7	2601.5
$Cu_{10}Al_4Mn_2$	This work	5070.3	2396.7	2696.9
$Cu_9Al_4Mn_3$	This work	5129.8	2485.8	2793.5
Cu_2AlMn	This work	5290.6	2690.6	3015.2
	(45), PAW	5272.9	2650.4	2972.3

Table 4: Calculated isotropic longitudinal, transversal and average sound velocities.

Alloy	Ref.	$v_l\langle 100 \rangle$	$v_t\langle 100 \rangle$	$v_l\langle 110 \rangle$	$v_t\langle 110 \rangle$	$v_l\langle 111 \rangle$	$v_t\langle 111 \rangle$
Cu_3Al	This work	4376.6	3718.9	5687.1	1133.2	6061.3	2244.6
$Cu_{11}Al_4Mn$	This work	4393.4	3749.4	5704.0	1284.4	6078.4	2288.2
$Cu_{10}Al_4Mn_2$	This work	4436.7	3717.5	5681.3	1566.2	6039.4	2398.0
$Cu_9Al_4Mn_3$	This work	4463.9	3822.4	5757.5	1665.9	6128.4	2407.3
Cu_2AlMn	This work	4595.7	3939.8	5878.4	2042.7	6247.7	2562.2
	(45), PAW	4576.2	3942.1	5882.5	1938.2	6257.7	2536.1
	(42), Exp	4553	3787	5670	— — —	6003	— — —

Table 5: Calculated anisotropic sound velocities.

The quotient between the bulk modulus and the shear modulus gives an idea about the ductility of the material. If this quotient is greater than 1.75, it is said that the material is ductile (60). According to this classification and the results shown in Table 2, all the studied alloys are predicted to show a ductile character. The Cauchy relation among C_{12} and C_{44} is also given in Table 2. This ratio indicates whether the interatomic forces are central or noncentral: if the quotient is equal to 1 the forces are central (61).

The calculated Debye temperatures at the equilibrium volume, $\Theta_{D,0} = \Theta_D(V_0)$ are shown in the last column of Table 2. It can be seen that the Debye temperature increases with the Mn content; this is consistent with the corresponding decrease of the Poisson ratio. For Cu_2AlMn , our result (378.18 K) can be compared with the experimental values found in the literature: Fenander et al. (62) obtained the value of 330K using calorimetric techniques, whereas in Ref. (42) a value of 372K was obtained by means of neutron scattering measurements. From the theoretical side, a value of 375.40K was obtained by Wen et al. (45).

From the elastic constants it is also possible to calculate the isotropic longitudinal, v_l , and transverse, v_t , components of the sound velocity as:

$$\rho v_l^2 = B_0 + \frac{4}{3}G_H \quad (17)$$

$$\rho v_t^2 = G_H \quad (18)$$

and its effective or average value

$$v_{eff} = \left[\frac{1}{3} \left(\frac{1}{v_l^3} + \frac{2}{v_t^3} \right) \right]^{-1/3} \quad (19)$$

The obtained results are given in Table 4. For Cu_2AlMn our results compare well with calculations presented in (45).

The velocities of longitudinal and transverse elastic waves in the direction $\langle 100 \rangle$, $\langle 110 \rangle$ and $\langle 111 \rangle$ for cubic crystals can be calculated by means of the second order elastic constant and the mass density ρ , using the relations (63):

$$\begin{aligned} v_l \langle 100 \rangle &= \sqrt{\frac{C_{11}}{\rho}} \\ v_t \langle 100 \rangle &= \sqrt{\frac{C_{44}}{\rho}} = v_{t_1} \langle 110 \rangle \\ v_l \langle 110 \rangle &= \sqrt{\frac{C_{11} + C_{12} + 2C_{44}}{2\rho}} \\ v_{t_2} \langle 110 \rangle &= \sqrt{\frac{C_{11} - C_{12}}{\rho}} \\ v_l \langle 111 \rangle &= \sqrt{\frac{C_{11} + 2C_{12} + 4C_{44}}{3\rho}} \\ v_t \langle 111 \rangle &= \sqrt{\frac{C_{11} - C_{12} + C_{44}}{3\rho}} \end{aligned}$$

The obtained values, and a comparison with recent calculations by (45) and experimental values from (42) are given in Table 5. As a general trend, both the average and the anisotropic sound velocities increase as the Mn content does. In particular, the $v_t \langle 110 \rangle$ is sensibly lower for Cu_3Al than for Cu_2AlMn , even though for the remaining directions the speeds do not differ markedly. The values obtained in this work for the directional velocities in Cu_2AlMn are in good agreement with the values calculated in (45), although slightly overestimate the experimental values from (42).

3.2 Thermal properties

The thermal properties of the alloys, between 0 and 600 K , were studied by means of the quasi-harmonic approximation detailed in Subsection 2.3. The variation of the isothermal bulk modulus in function of temperature for the different alloys is shown in Fig. 6. Experimental values for Cu_2AlMn obtained from the literature are included for comparison (42, 64). The calculated values overestimate the experimental ones from Ref. (42) by less than 5% at low temperatures, but the differences reduce as room temperature is approached.

The thermal variation of the Debye temperature for the different alloys is show in Fig. 7. The experimental data from Ref. (42, 62) for Cu_2AlMn are included for comparison; our results are in good agreement with the measurements by Michelluti et al (42) It can be seen that the Θ_D is almost invariable when $T < 100K$. For greater temperatures than $T = 100$ the Θ_D decreases.

Thermal expansion is an important phenomenon in the thermodynamics of materials. It is interesting to analyze the behavior of the lattice parameter as a function of temperature. This is displayed in Fig. 9 for the different alloys considered in this work. The slopes of the lattice parameters are very similar for the different compositions; there are not remarkable difference between the predicted thermal variation of the lattice parameters for Cu_3Al and for Cu_2AlMn . The values of the thermal expansion coefficient at room temperature are $5.79 \times 10^{-5} K^{-1}$ for Cu_3Al and $6.06 \times 10^{-5} K^{-1}$ for Cu_2AlMn .

In Fig. 9 the lattice parameters at room temperature are plotted as a function of the alloy composition. The lattice parameter increases with the Mn content in an approximately linear way. Also included in Fig. 9 are the experimental

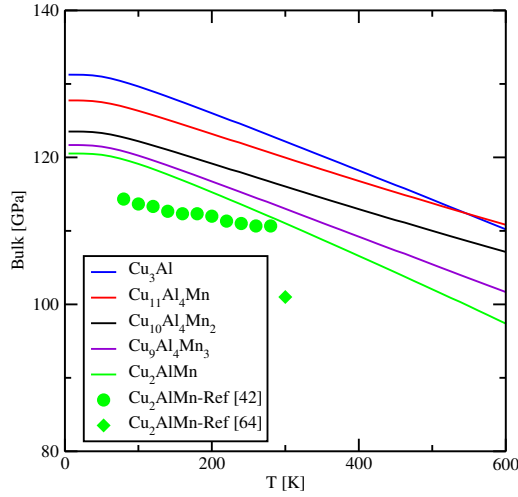


Figure 6: Thermal variation of the bulk modulus for different compositions

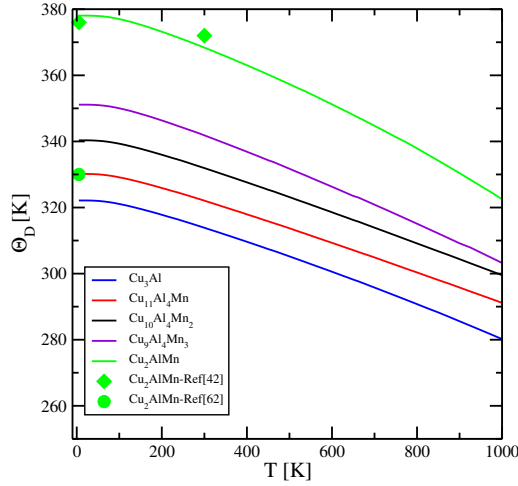


Figure 7: Thermal variation of the Debye temperature for different compositions. The experimental values for Cu_2AlMn are represented with diamonds (42) and circles (62).

data from Refs. (20, 65). Our results slightly overestimates the experimental values; the maximum difference is below 1% in the Cu-rich corner and gradually reduces for higher Mn content.

4 Conclusions

In this work, the elastic constants of $Cu - Al - Mn$ alloys with structure derived from the bcc, and located along the pseudo-binary line $Cu_3Al \rightarrow Cu_2AlMn$, have been determined by first-principles calculations. Our results present good agreement with both experimental and theoretical values reported in the bibliography. Although the equilibrium volume of the different alloys smoothly increases with the manganese content, the elastic constants C_{11} and C_{44} do not display remarkable composition dependence. A more noticeable change is found in the behavior of C_{12} , which steadily

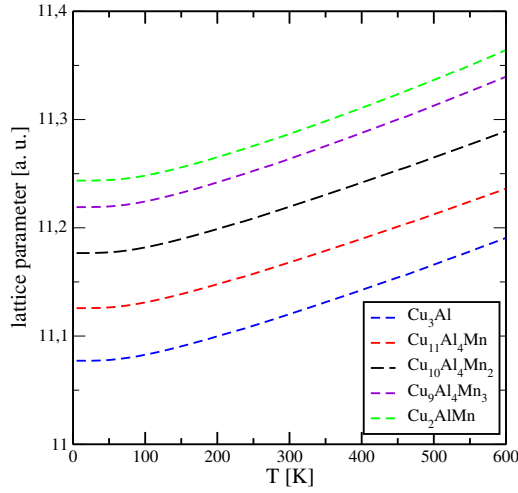


Figure 8: Lattice parameter for the alloys at different temperatures.

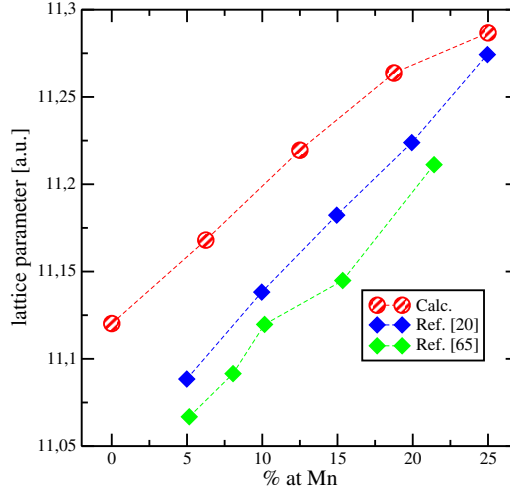


Figure 9: Lattice parameter for the alloys at room temperature and comparison with experimental data

decreases with the Mn content. For the alloys with lower Mn content the constant C' is smaller, and the alloys become more susceptible to structural changes under compression in direction $\langle 110 \rangle$ (51). From the aforementioned elastic constants, other quantities of interest for the structural behavior of the alloy, such as Young's modulus, shear modulus and Poisson's ratio, have been obtained.

The anisotropy has, in general, large values for all the studied alloys, being lower for Cu_2AlMn and increasing as the copper content grows. This would facilitate both spinodal decomposition and martensitic transformation (51, 57, 58). The directional Poisson's ratio for loads in the $[110]$ direction have been calculated. For strains along the transverse $[1\bar{1}0]$ direction a negative Poisson's ratio is predicted, whereas for strains along $[100]$, the Poisson ratio is positive and greater than unity. These results agree with a recent experimental work (56).

The isotropic and directional sound velocities have been calculated from the elastic constants. Both values agree well with the known results for $L2_1 - Cu_2AlMn$.

Finally, the behaviour of the bulk modulus, Debye temperature and equilibrium lattice parameter as a function

of temperature has been calculated through the Quasi-harmonic approximation. According with our calculations, the difference between the lattice parameter of Cu_3Al and Cu_2AlMn does not change significantly with the temperature. The agreement with experimental results has been found to be satisfactory(42, 62, 64).

Acknowledgment

The authors thank to UNCPBA, ANPCyT (PICT 2017–4062) and CONICET (Argentina) for their financial support, and to Dr. R. Romero (IFIMAT-UNCPBA) for helpful suggestions. A.A. thanks the post-doctoral fellowship from CONICET.

References

1. J. M. Jani, M. Leary, A. Subic, M. A. Gibson, *Materials & Design (1980-2015)* **56**, 1078–1113 (2014).
2. L. Delaey, *Materials Science and Technology, Vol. 5 Phase Transformations in Materials*, edited by P. Haasen VCH, 1991.
3. Y. Sutou, T. Omori, R. Kainuma, K. Ishida, *Materials Science and Technology* **24**, 896–901 (2008).
4. Y. Araki *et al.*, *Earthquake Engineering & Structural Dynamics* **40**, 107–115 (2011).
5. F. Hosseini, B. Gencturk, S. Lahpour, D. I. Gil, *Smart Materials and Structures* **24**, 085029 (2015).
6. J.-L. Liu, H.-Y. Huang, J.-X. Xie, *Materials & Design* **85**, 211–220 (2015).
7. H. Aslani, C. Cabrera, M. Rahnama, *Earthquake Engineering & Structural Dynamics* **41**, 1549–1568 (2012).
8. K. C. Shrestha *et al.*, presented at the Sensors and Smart Structures Technologies for Civil, Mechanical, and Aerospace Systems 2012, vol. 8345, 83452K.
9. Y. Araki *et al.*, *Structural Control and Health Monitoring* **21**, 1304–1315 (2014).
10. W.-S. Chang, Y. Araki, presented at the Proceedings of the Institution of Civil Engineers-Civil Engineering, vol. 169, pp. 87–95.
11. J. Oliveira *et al.*, *Materials & Design* **90**, 122–128 (2016).
12. S. Pareek, Y. Suzuki, Y. Araki, M. Youssef, M. Meshaly, *Engineering Structures* **175**, 765–775 (2018).
13. S. Konoplyuk, V. Kokorin, O. Kolomiets, A. Perekos, V. Nadutov, *Journal of Magnetism and Magnetic Materials* **323**, 763–766 (2011).
14. M. Bouchard, R. Livak, G. Thomas, *Surface Science* **31**, 275–295 (1972).
15. E. Obradó, L. Mañosa, A. Planes, R. Romero, A. Somoza, *Materials Science and Engineering: A* **273**, 586–589 (1999).
16. K. Sato, W. Stobbs, *Philosophical Magazine A* **69**, 349–377 (1994).
17. J. Marcos, L. Mañosa, A. Planes, R. Romero, M. L. Castro, *Philosophical Magazine* **84**, 45–90 (2004).
18. D. Velazquez, R. Romero, *Journal of Thermal Analysis and Calorimetry* **130**, 2007–2013 (2017).
19. D. Oxley, R. Tebble, K. Williams, *Journal of Applied Physics* **34**, 1362–1364 (1963).
20. R. Kainuma, N. Satoh, X. Liu, I. Ohnuma, K. Ishida, *Journal of Alloys and Compounds* **266**, 191–200 (1998).
21. Y. Kudryavtsev *et al.*, *Journal of applied physics* **97**, 113903 (2005).
22. B. Dubois, D. Cheverreau, *Journal of Materials Science* **14**, 2296–2302 (1979).

23. D. Velázquez, M. Chaparro, H. Böhnelt, R. Romero, F. Lanzini, *Materials Chemistry and Physics*, 122793 (2020).
24. F. Lanzini, A. Alés, *Journal of Magnetism and Magnetic Materials* **395**, 234–239 (2015).
25. P. Giannozzi *et al.*, *Journal of physics: Condensed matter* **21**, 395502 (2009).
26. P. Giannozzi *et al.*, *Journal of Physics: Condensed Matter* **29**, 465901 (2017).
27. P. Hohenberg, W. Kohn, *Phys. Rev.* **136**, B864–B871 (3B November 1964).
28. W. Kohn, L. J. Sham, *Phys. Rev.* **140**, A1133–A1138 (4A November 1965).
29. D. Vanderbilt, *Physical review B* **41**, 7892 (1990).
30. J. P. Perdew, K. Burke, M. Ernzerhof, *Phys. Rev. Lett.* **77**, 3865–3868 (18 October 1996).
31. H. J. Monkhorst, J. D. Pack, *Physical review B* **13**, 5188 (1976).
32. A. Deb, Y. Sakurai, *Journal of Physics: Condensed Matter* **12**, 2997 (2000).
33. E. Zukowski *et al.*, English, *Journal of Physics Condensed Matter* **9**, Cited By :25, 10993–11005 (1997).
34. F. D. Murnaghan, *Proceedings of the National Academy of Sciences* **30**, 244–247, ISSN: 0027-8424 (1944).
35. M. Mehl, J. Osburn, D. Papaconstantopoulos, B. Klein, *Physical Review B* **41**, 10311 (1990).
36. H. Rached, D. Rached, R. Khenata, A. H. Reshak, M. Rabah, *physica status solidi (b)* **246**, 1580–1586 (2009).
37. R. Hill, *Journal of the Mechanics and Physics of Solids* **11**, 357–372 (1963).
38. W. Voigt *et al.*, *Lehrbuch der kristallphysik* (Teubner Leipzig, 1928), vol. 962.
39. A. Reuss, *ZAMM-Journal of Applied Mathematics and Mechanics/Zeitschrift für Angewandte Mathematik und Mechanik* **9**, 49–58 (1929).
40. M. Blanco, E. Francisco, V. Luana, *Computer Physics Communications* **158**, 57–72 (2004).
41. E. Francisco, J. Recio, M. Blanco, A. M. Pendás, A. Costales, *The Journal of Physical Chemistry A* **102**, 1595–1601 (1998).
42. B. Michelutti, R. P. de La Bathie, E. d. T. de Lacheisserie, A. Waintal, *Solid State Communications* **25**, 163–168 (1978).
43. S.-C. Wu, G. H. Fecher, S. Shahab Naghavi, C. Felser, *Journal of Applied Physics* **125**, 082523 (2019).
44. J. Jalilian, *Journal of Alloys and Compounds* **626**, 277–279 (2015).
45. Y. Wen *et al.*, *Journal of Superconductivity and Novel Magnetism* **31**, 1847–1856 (2018).
46. A. Prasetyo, F. Reynaud, H. Warlimont, *Acta Metallurgica* **24**, 651–658 (1976).
47. A. Planes, L. Mañosa, E. Vives, *Physical Review B* **53**, 3039 (1996).
48. L. Mañosa *et al.*, *Physical Review B* **49**, 9969 (1994).
49. R. Romero, J. Pelegrina, *Materials Science and Engineering: A* **354**, 243–250 (2003).
50. A. Planes, L. Mañosa, in *Solid state physics* (Elsevier, 2001), vol. 55, pp. 159–267.
51. B. Verlinden, T. Suzuki, L. Delaey, G. Guenin, *Scripta metallurgica* **18**, 975–979 (1984).
52. C. Zener, *Phys. Rev.* **71**, 846–851 (12 June 1947).
53. Z. A. Lethbridge, R. I. Walton, A. S. Marmier, C. W. Smith, K. E. Evans, *Acta Materialia* **58**, 6444–6451 (2010).

54. K. Evans, M. Nkansah, *Nature* **353**, 124 (1991).
55. R. H. Baughman, J. M. Shacklette, A. A. Zakhidov, S. Stafström, *Nature* **392**, 362 (1998).
56. S. Xu *et al.*, *Scripta Materialia* **177**, 74–78 (2020).
57. J. W. Cahn, *Acta metallurgica* **9**, 795–801 (1961).
58. J. W. Cahn, *Acta metallurgica* **10**, 179–183 (1962).
59. M. Bouchard, G. Thomas, *Acta metallurgica* **23**, 1485–1500 (1975).
60. S. Pugh, *The London, Edinburgh, and Dublin Philosophical Magazine and Journal of Science* **45**, 823–843 (1954).
61. D. Pettifor, *Materials science and technology* **8**, 345–349 (1992).
62. N. Fenander, L. Wiktorin, H. Myers, *Journal of Physics and Chemistry of Solids* **29**, 1973–1976 (1968).
63. R. Truell, C. Elbaum, B. B. Chick, *Ultrasonic methods in solid state physics* (Academic press, 2013).
64. M. L. Green, G. Chin, J. Vander Sande, *Metallurgical Transactions A* **8**, 353–361 (1977).
65. S. Sugimoto *et al.*, *Journal of alloys and compounds* **265**, 273–280 (1998).